Eidgenössische Technische Hochschule Zürich
Swiss Federal Institute of Technology Zurich

Justus Urbanetz
23-942-246

Inhibition of decay channels for alkaline-earth circular Rydberg atoms between two parallel conducting plates

Semester Thesis

Master's Degree Programme in Physics
Trapped Ion Quantum Information Group (TIQI)
Swiss Federal Institute of Technology (ETH) Zurich

Supervision

Wojciech Adamczyk, Silvan Koch, Dr. Claudia Politi
Prof. Dr. Jonathan Home

June, 2024

Abstract

This thesis explores the lifetime of circular Rydberg (cRy) atoms in free space, starting with an analysis of hydrogen-like atoms using the Coulomb approximation. It covers the eigenfunctions and eigenenergies of hydrogen, introducing quantum defects and fine structure perturbations. The study then extends to Rydberg states, emphasizing circular states in alkali and alkaline-earth atoms, and considers their behavior in external electric fields. Using Fermi's golden rule, the decay rates and lifetimes of cRy states are derived, demonstrating significant longevity, especially at cryogenic temperatures. Additionally, the effects of spontaneous emission inhibition between conducting plates are analyzed, revealing enhanced or suppressed decay rates depending on the polarization and distance between the plates. The findings suggest promising avenues for future research into geometries and materials that influence the density of supported modes in circular Rydberg state settings.

Acknowledgements

Firstly, I would like to express my heartfelt gratitude to Wojciech Adamczyk, Silvan Koch, and Dr. Claudia Politi for their invaluable supervision, unwavering support, and extensive knowledge. Your guidance provided profound insights into exciting areas of physics and consistently inspired me with your creative thinking. Your constructive feedback was instrumental in the completion of this thesis. I thoroughly enjoyed working alongside you and eagerly anticipate writing my master's thesis under your mentorship. Thank you very much!

I would also like to extend my gratitude to Ian Le Meur for his engaging discussions about electromagnetic fields in the presence of conducting media. His explanations greatly enhanced my understanding and made this aspect of the project much more enjoyable.

Finally, I am deeply grateful to Prof. Jonathan Home for offering me the opportunity to work on this project within his group. His active participation and guidance during our weekly Rydberg group meetings were crucial in maintaining the project's focus and driving its development.

Contents

Chapter 1

Introduction

Among cold atoms, those excited to very energetic states deserve special attention. Typically associated with high principal quantum number $n \gg 1$, they are called Rydberg states. Due to their high sensitivity to external fields and strong dipolar interactions, Rydberg atoms play a crucial role in the development of quantum technologies. Great results have been achieved using ultracold Rydberg atoms, ranging from quantum sensors [1] to high-fidelity qubit entanglement [2]. Furthermore, it was possible to simulate the antiferromagnetic two-dimensional Ising model [3]. In these implementations, the qubit is encoded in the long-lived hyperfine levels of the atom. In this case, to implement interactions between two qubits, they need to be excited to Rydberg states, which have high decay rates. In a zero-temperature environment, the lifetimes are typically on the order of microseconds due to the emission of photons in the optical regime, thus limiting the coherence time [4]. This is a limiting factor when higher gate fidelities are desired.

In the search for states with longer lifetimes, circular Rydberg states can be considered. They are characterized by their maximal angular momentum $l = |m_l| = n-1$. Using rapid adiabatic passage circular Rydberg states can be created from Rydberg states with low orbital momentum as outlined by Haaiteng Wu in Ref. [5]. Their maximal angular momentum restricts the number of possible decay channels, leading to intrinsically longer lifetimes. For a zero-temperature environment, there is only a single decay channel due to spontaneous emission of a photon to the next lower circular Rydberg state. The wavelength of a photon corresponding to this transition is in the millimeter range, resulting in a lifetime on the order of several milliseconds, which is approximately an order of magnitude longer than at room temperature [5]. Groups working with circular Rydberg states have proposed implementing a structure, using various geometries and materials, that inhibits the decay of the state through spontaneous inhibition [5–8]. Using such a structure could potentially boost the lifetime of circular Rydberg states in cryogenic environments to the order of seconds [7, 9].

Our group is building an experimental cryogenic setup aiming at non-destructive readout of individual circular Rydberg states of ^{40}Ca atoms. This setup allows circular Rydberg states to be used in quantum simulation and computation. Using an alkaline-earth atom allows for the cooling and trapping of the atoms in tweezers by exploiting the optically active valence electron [10]. The readout will be based on a scheme for alkaline-earth atoms developed by Christoph Fischer in his Ph.D. thesis [11] and proposed by Andrea Muni et al. in Ref. [12]. This thesis should work as a basis for implementing a spontaneous inhibition apparatus into the setup to increase the atom's lifetime. Figure 1.1 schematically shows the trapped circular atoms, denoted as red circles, inside the spontaneous inhibition setup, which in this case is shown as two parallel plates with separation d. Another crucial aspect of the inhibition structure is that the optical tweezers, shown as green bi-conical shapes in Fig. 1.1, maintain their integrity when moved into the geometry. In a broader context, the inhibition structure should still permit optical access. This ensures that the trapping of the atoms is not compromised.

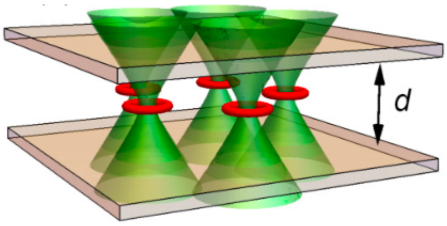

Figure 1.1: Circular Rydberg states (indicated as red circles) trapped in optical tweezers (indicatd as green bi-conical shapes), while kept inside an inhibition structure separated by a distance d. This figure is adapted from the work of Florian Meinert [8].

Decay processes governing the lifetime of an atom can be calculated quantum mechanically with Fermi's golden rule. The rate of decay is given by the overlap of the wave functions of the initial and final state with a perturbation operator connecting the two. Therefore, a discussion of involved states and the interaction Hamiltonian is necessary.

In Chapter 2, the lifetime of alkaline-earth circular Rydberg states will be discussed as we use ^{40}Ca for our experiment. To calculate properties such as the lifetime of circular Rydberg states, we require wave functions to describe them. We will begin by discussing the wave function and energy structure of the hydrogen atom, focusing on the Hamiltonian for an electron in the Coulomb potential. Rydberg states of alkali atoms involve a single valence electron excited to a high principal quantum number n, resulting in an orbit with a radius on the order of nm [13]. We derive the treatment of these Rydberg states based on the hydrogen atom, incorporating the more complex electronic structure through the use of the quantum defect. In the following part, circular Rydberg states, are derived. We discuss the analogous treatment to the hydrogen atom and the effect of the quantum defect. Finally, we derive the wave functions and the energy splitting between two neighboring circular states. Furthermore, the degeneracy in the quantum numbers l and m_l due to the Coulomb potential is addressed. To stabilize degenerate circular Rydberg states, an external electric field is applied, resulting in an additional potential. Consequently, this leads to an energy shift and the emergence of new good quantum numbers, which are discussed.

The lifetime for an atom in free space is determined by its coupling to the continuum of radiation modes of the electric field, as discussed in Chapter 2, which give rise to different decay mechanisms. In 1946, Edward Purcell et al. predicted the modification of one of the processes, the spontaneous emission. In the context of nuclear magnetic resonance, they predicted an enhanced rate of decay due to spontaneous emission [14]. Later in 1981, Daniel Kleppner et al. proposed experiments to inhibit spontaneous decay of atoms inside a cavity completely [15]. Their approach involved modifying the density of modes resonant with the atomic transition frequency using two parallel conducting plates. Consequently, when the modes that support the decay mechanism are suppressed, the decay rate is reduced or, in extreme cases, completely inhibited.

For circular Rydberg states, the lifetime will be shown to be strongly temperature-dependent. Thus, experiments usually are constrained to cryogenic environments. By using a cryogenic environment, stimulated decay can largely be inhibited due to the absence of black-body radiation. However, spontaneous decay is temperature-independent and can be understood as a coupling of the dipole moment of the atom to the vacuum fluctuations of the electric field. By placing the atom in a cavity-like system, first realized by Hulet et al. in 1985, even the spontaneous emission could be suppressed [6]. The implemented cavity-like structure modifies the density of supported electric field modes, by suppressing the modes through which the atom can spontaneously decay. Inhibiting this channel effectively while maintaining cryogenic temperatures, the lifetime of circular Rydberg states can be increased significantly [16]. A proposal for using a waveguide-like structure leads to an even better inhibition of decay promising lifetimes on the order of seconds [9].

In this chapter, we will explore how the decay rate of a circular Rydberg state changes when positioned between two conducting plates. One approach involves solving Maxwell's equations to address the scenario with perfectly conducting plates. Another approach employs the method of image charges, which provides solutions for both perfect and imperfect conductors. Using the expression for the modified electric field between the conductors, the change in decay rate compared to free space for circular Rydberg states will be deduced. We will analyze and compare the results for the case of perfect and imperfect mirrors. From this analysis we will see that the factors of inhibition are polarization dependent and vary for different spacings between the conductors.

Chapter 2

Lifetime of cRy atoms in free space

2.1 Coulomb approximation of hydrogen atom

Hydrogen has the simplest structure of all atoms, consisting of just one electron and one proton coupled by Coulomb interaction. Therefore, it is one of the few two-particle problems in quantum physics with an analytical solution. The Hamiltonian for the hydrogen atom reads [17]:

$$H_0 = -\frac{\hbar^2}{2m_{\text{red}}}\nabla^2 - \frac{q_e^2}{4\pi\epsilon_0}\frac{1}{r}. \tag{2.1}$$

Above, $m_{\text{red}} = \frac{m_{\text{e}}}{1+m_{\text{e}}/m_{\text{core}}}$ is the reduced mass, where m_{e} and m_{core} respectively denote the mass of the electron and the core. q_{e} denotes the charge of an electron, and ϵ_0 is the vacuum permittivity. The eigenfunctions to the Hamiltonian are known to be a product of radial and angular functions in spherical coordinates [17]:

$$\psi_{n,l,m_l}(r,\theta,\phi) = R_{nl}(r)Y_l^{m_l}(\theta,\phi). \tag{2.2}$$

The radial $R_{nl}(r)$ and angular $Y_l^{m_l}(\theta,\phi)$ functions are defined as [17]:

$$\begin{aligned} &Y_l^{m_l}(\theta,\phi) \propto e^{im_l\phi}P_l^{m_l}(\cos\theta), \\ &R_{n,l}(r) = \sqrt{\left(\frac{2}{na_0}\right)^3 \frac{(n-l-1)!}{2n[(n+l)!]}}\, e^{-r/na_0}\left(\frac{2r}{na_0}\right)^l L_{n-l-1}^{2l+1}\left(\frac{2r}{na_0}\right), \end{aligned} \tag{2.3}$$

where $a_0 \approx 5.29 \times 10^{-11}$ m is the Bohr radius. An eigenstate of H_0 is defined by its quantum numbers, namely the principal quantum number $n > 0$, the orbital angular momentum number l, and the magnetic quantum number m_l. The latter two are defined with respect to the quantization axis. For a state with principal quantum number n, the following configurations of l and m_l are allowed [17]:

$$l = 0, 1, 2, ..., n-1, \tag{2.4}$$

$$m_l = -l, -l+1, ..., -1, 0, 1, ..., l-1, l. \tag{2.5}$$

The corresponding eigenenergies are degenerate in the l and the m_l quantum number [17]:

$$E_n = -\frac{q_e^2}{8\pi\epsilon_0 a_0}\frac{1}{n^2}, \tag{2.6}$$

$$= -\mathrm{Ry}\frac{1}{n^2}. \tag{2.7}$$

$\mathrm{Ry} \approx -13.6\mathrm{eV}$ is known as the Rydberg constant. The structure resulting from the n-dependent calculation of energy in Eq. 2.7 is known as the gross structure. The energy of a photon reads $E_{\mathrm{ph}} = h\omega$. Therefore, the energy difference between two neighboring n states translates to a frequency $\omega_{n,n-1}$ of a photon:

$$\omega_{n,n-1} = \frac{1}{h}|E_n - E_{n-1}|, \tag{2.8}$$

$$= \frac{\mathrm{Ry}}{h}\frac{2n-1}{n^2(n-1)^2}. \tag{2.9}$$

This problem statement is ideal for addressing atoms that resemble hydrogen. More precisely, this means states which can be approximated to have a single valence electron in the potential of a single positive charge.

2.2 Hyperfine structure

A deeper consideration of the energy structure yields the fine structure of atoms, which is not specific to hydrogen but generally applies to all atomic species. The fine structure accounts for spin-orbit interaction H_{SO}, the correction due to relativistic effects H_{REL}, and the Darwin term H_{D}. The according Hamiltonian reads:

$$H_{\mathrm{FS}} = H_{\mathrm{SO}} + H_{\mathrm{REL}} + H_{\mathrm{D}}. \tag{2.10}$$

First, we want to treat the spin-orbit interaction. In the rest frame of the valence electron, the nucleus and inner electronic shells orbit around the electron. This generates a magnetic field $\mathbf{B}$. The spin of the electron, denoted by the operator $\mathbf{S}$, generates a magnetic moment $\mu = -\frac{q_{\mathrm{e}}}{m_{\mathrm{e}}c}\mathbf{S}$. The interaction reads:

$$H_{\mathrm{SO}} = -\frac{1}{2}\mu \cdot \mathbf{S}. \tag{2.11}$$

We will now skip a few steps because they do not add to the following discussions. A detailed discussion can be found in lecture notes from Barton Zwiebach [18]. The above Hamiltonian can be rewritten as follows [19]:

$$H_{\mathrm{SO}} = \frac{1}{2m_{\mathrm{e}}^2c^2}\frac{1}{r}\frac{dV}{dr}\mathbf{L}\cdot\mathbf{S}, \tag{2.12}$$

where $\mathbf{L} = \mathbf{r} \times \mathbf{p}$ is the operator for angular momentum and $V = -\frac{Zq_{\mathrm{e}}^2}{r}$ denotes the potential of nucleus with Z protons. Another term appearing in the fine structure Hamiltonian is the correction due to relativistic effects. The relativistic energy of a particle with mass m and momentum p can be written as:

$$\sqrt{m^2c^4 + c^2p^2} = mc^2 + \frac{p^2}{2m} - \frac{p^4}{8m^3c^2} + \dots, \tag{2.13}$$

where we expanded the square root in powers of momentum under the assumption $p \ll mc$. The first term on the right-hand side is the rest energy, the second term is the kinetic energy, while the third term accounts for relativistic corrections leading to [19]:

$$H_{\mathrm{REL}} = -\frac{p^4}{8m^3c^2}. \tag{2.14}$$

The Darwin term is harder to interpret. It accounts for the uncertainty of the electron-position during its interaction with the potential of the nucleus. The Hamiltonian describing the correction reads [19]:

$$H_{\mathrm{D}} = \frac{1}{8}\frac{\hbar^2}{m^2c^2}\nabla^2 V. \tag{2.15}$$

In analyzing the fine structure perturbation, we encounter that $\mathbf{L}$ and $\mathbf{S}$ do not commute with H_{FS}, to be precise with $H_{\mathrm{SO}} \propto \mathbf{L}\cdot\mathbf{S}$. Therefore, we introduce the total angular momentum:

$$\mathbf{J} = \mathbf{L} + \mathbf{S}, \tag{2.16}$$

and calculate the commutation relation of each of the components of the fine structure with $\mathbf{L}, \mathbf{L}^2, \mathbf{S}, \mathbf{S}^2, \mathbf{J}, \mathbf{J}^2$. The results are given in Table 2.1, where ✓ denotes two operators which commute while ✗ denotes the opposite [18].

	L	L^2	S	S^2	J	J^2
H_{RKE}	✓	✓	✓	✓	✓	✓
H_D	✓	✓	✓	✓	✓	✓
H_{SO}	✗	✓	✗	✓	✓	✓

Table 2.1: The table indicates whether an operator commutes with a term of the fine structure Hamiltonian. A ✓ at the field of two operators indicates that they commute, a ✗ indicates they do not.

One can see that H_{FS} is diagonal in the basis of $\mathbf{L}^2, \mathbf{S}^2, \mathbf{J}, \mathbf{J}^2$, while the fine structure Hamiltonian does not commute with $\mathbf{L}$and$\mathbf{S}$. The resulting energy shift in the diagonal basis reads:

$$\Delta E_{\mathrm{FS}} = \frac{E_n(Z\alpha)^2}{n^2}\left(\frac{n}{j+1/2} - \frac{3}{4}\right). \tag{2.17}$$

In conclusion, the fine structure Hamiltonian introduces a term $\mathbf{L}\cdot\mathbf{S}$, which does not commute with $\mathbf{L}$ and $\mathbf{S}$, the operators used to describe the gross structure. To this end, a new operator, $\mathbf{J} = \mathbf{L} + \mathbf{S}$, is introduced to describe the total angular momentum. This operator accounts for the energy shifts due to fine structure considerations.

2.3 Rydberg states

Rydberg atoms are highly excited atomic states with one or more valence electrons in orbits of high principal quantum number n, while the inner electrons are in their ground state close to the core. Assuming a neutral atom with one electron in a Rydberg state, the Coulomb attraction of Z positive charges of the core is shielded by $Z-1$ inner electrons. Therefore, the Rydberg electron experiences a near-hydrogenic potential, and thus its gross structure can be treated similar to hydrogen.

In the first subsection, we will discuss the properties of atoms with a single valence electron, the alkali atoms. To provide a good understanding of Rydberg states with maximal angular momentum $l=|m_l|=n-1$, the so-called circular states, the energy structure and the wave function properties will be discussed. The focus of the following subsection is alkaline-earth atoms. The main difference to alkali atoms is the presence of a second valence electron. This introduces an interaction term between the two valence electrons, changing the structure of the problem. However, it will be shown that for an electronic configuration where one electron is kept close to the ground state and the other is brought to a circular Rydberg state, the interaction between the two can be neglected to first order.

2.3.1 Alkali atoms

In this subsection, we investigate both low- and high-l states of alkali Rydberg states. For states with low orbital momentum, the discussion is based on the gross structure of hydrogen from Sec. 2.1 and the fine structure from Sec. 2.2. Furthermore, the quantum defect will be introduced to account for energy corrections to the gross structure of hydrogen. The description of Rydberg states of high orbital momentum will be shown to be approximated by hydrogen, especially in the circular state, while the corrections to the energy discussed for low-l states can be neglected.

States of low orbital momentum l

An electron's state can be approximated as hydrogen-like if it experiences a potential similar to that of a single positive charge at the center of its orbit. In alkali atoms, this approximation holds when the inner electron cloud, with a charge of $Z-1$, effectively screens the nucleus's Z positive charges from the valence electron. This scenario occurs when the valence electron's orbit is sufficiently distant from the nucleus and inner electron shells, collectively referred to as the ionic core. At this distance, the Rydberg electron perceives the ionic core as a single positive charge, allowing it to be modeled by the gross structure of hydrogen. However, when the Rydberg electron approaches the ionic core and penetrates the inner electron shells, necessary energy corrections must be applied. Fig. 2.1 schematically illustrates the radial orbit of an electron as a function of l. Consequently, for low orbital momentum states, the orbit becomes more elliptical and eccentric. This implies that for states with low orbital momentum, the Rydberg electron experiences a deeper potential than that predicted by the hydrogen model. The quantum defect δ_{nlj} accounts for the deviation from the ideal Coulomb potential by modifying the gross structure in Eq. 2.7, which then becomes:

$$E_{n,l,j}=-\frac{q_e^2}{8\pi\epsilon_0 a_0}\frac{1}{1+m_\mathrm{e}/m_\mathrm{core}}\frac{1}{(n-\delta_{nlj})^2}. \tag{2.18}$$

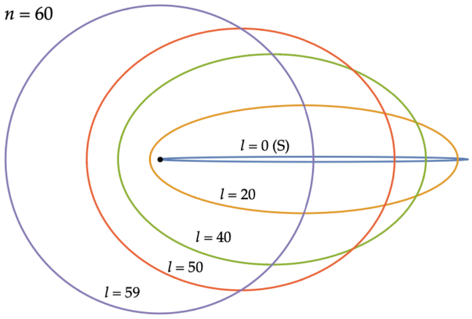

Figure 2.1: Radial electronic orbit for $l = 0, 20, 40, 50, 59$ in the hydrogen atom with principal quantum number $n = 60$. With increasing orbital momentum, the trajectory becomes more round and more centric. For $l = 59$, a perfectly circular orbit has been achieved. This is adopted from the PhD thesis of Thanh-Long Nguyen [20].

The quantum defect $\delta_{n,l,j}$ is defined by the Rydberg-Ritz formula [16]:

$$\delta_{nlj} = \delta_{lj}^{(0)} + \frac{\delta_{lj}^{(2)}}{\left(n - \delta_{lj}^{(0)}\right)^2} + \frac{\delta_{lj}^{(4)}}{\left(n - \delta_{lj}^{(0)}\right)^4} + \cdots . \tag{2.19}$$

Since it accounts for the valence electron penetrating the ionic core of the nucleus and the inner electronic shells, it depends strongly on the angular momentum l, but not on n and j [16]. For states with $l \geq 4$, the quantum defect scales as [13]:

$$\delta_{l \geq 4} \propto l^{-5}. \tag{2.20}$$

Therefore, the quantum defect decreases exponentially as l increases. This observation is consistent with the schematic in Fig. 2.1, which shows that as l increases, the orbit of the Rydberg electron becomes more circular and centered. Consequently, fewer corrections are needed for the valence electron's penetration into the inner electron shells.

States of maximal orbital momentum l

Rydberg states with maximal angular momentum $l = |m_l| = n - 1$ are called circular Rydberg states (cRy). In the following, we will denote these states as $|nC\rangle = |n, l = n - 1, |m| = n - 1\rangle$. Their wave function can be derived from the wave function of hydrogen, see Eq. 2.2, using the appropriate quantum numbers and has the following form [21]:

$$\psi_{nC}(r, \theta, \phi) = \frac{1}{\sqrt{\pi a_0^3}} \frac{1}{nn!} \left(-\frac{r}{na_0} \sin\theta e^{i\phi} \right)^{n-1} e^{-r/na_0}. \tag{2.21}$$

As n increases, the factor $\sin^{n-1}\theta$ in Eq. 2.21 causes the electron to become increasingly confined to the plane where $\theta = \pi/2$. Additionally, when calculating the mean radius r_n of the orbit and

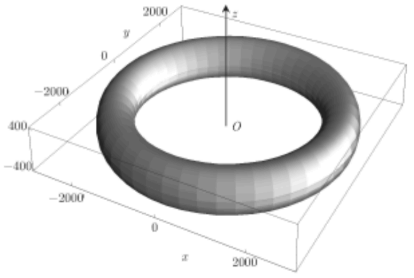

Figure 2.2: Showing the spatial probability distribution of the valence electron in $|50C\rangle$ of ^{87}Rb. The surface of the toroid indicates equal values (50% of the maximum value) for the spatial probability distribution $P = \int\int\int |\psi_{nC}(r,\theta,\phi)|^2 dV$. The dimensions are in units of the Bohr radius, a_0. This figure is adopted from 'Exploring the Quantum' by Serge Haroche [21].

its variance Δr_n for the electron, the following results are obtained:

$$r_n = a_0 n^2, \tag{2.22}$$

$$\Delta r_n = a_0 n^2/\sqrt{2n}. \tag{2.23}$$

Examining the ratio of these two quantities, we see:

$$\frac{r_n}{\Delta r_n} = \sqrt{2n}. \tag{2.24}$$

With increasing n, this ratio becomes larger, indicating stronger radial confinement. Combining the confinement in both angular and radial perspectives, this leads to a circular orbit for $n \to \infty$. These features can be observed by plotting the probability density distribution of $|50C\rangle$ in ^{87}Rb, see Fig. 2.2.

We now examine the effect of the fine structure perturbation, see Eq. 2.17, for circular states of alkali atoms. Considering the expression for the total angular momentum in Eq. 2.16, the eigenvalues of this operator are given by $j = l \pm s$, which in the case of a single electron, as in alkali atoms, translates to:

$$j = l \pm \frac{1}{2}. \tag{2.25}$$

In the case of large principal quantum number n, one can approximate $l \approx n$, and for alkali atoms with $s = \pm 1/2$, it is thus reasonable to write $j \approx n$, see Eq. 2.25. Therefore, the correction energy from the fine structure in circular states scales as:

$$\Delta E_{\text{FS}} \approx \frac{\alpha^2}{4n^2} E_n. \tag{2.26}$$

For states with $n \approx 50$, the fine structure energy shift ΔE_{FS} is on the order of kHz. This shift is negligible compared to the typical energy shifts experienced by circular Rydberg states under external electric or magnetic fields, which are on the order of MHz. Therefore, ΔE_{FS} will not be considered here. The influence of electric fields will be discussed in Sec. 2.4.

The previous subsection 2.3.1 mentioned a scaling law of $\delta_{l \geq 4} \propto l^{-5}$ for the quantum defect in terms of l. Therefore, as cRy states have $n \gg 1$ and maximal angular momentum $l = n - 1$, the quantum defect is negligible [16]. An intuitive reasoning can be found when looking at the radial wave function in Fig. 2.1, where the trajectory of a circular state does not come close to the core. In conclusion, states with large orbital momentum can be approximated by a hydrogen atom, whith cRy states are the ideal case. The energy structure of circular Rydberg states follows the gross structure of in Eq. 2.7, and corrections due to the fine structure, see Eq. 2.17, and the quantum defect, see Eq. 2.18, can be neglected.

2.3.2 Circular Rydberg states of alkaline-earth atoms

In contrast to the previous discussion on alkali atoms, this subsection focuses on alkaline-earth atoms, which have a second valence electron. These two electrons interact through Coulomb repulsion. We aim to explore the effects when one valence electron is in a circular Rydberg state and the other remains optically active, i.e. near the ground state. The following discussion is based on the one presented in the PhD thesis of Christoph Fischer [11]. Consider the simplest case of two electrons in the potential of a nucleus with charge $Z = 2$. Each electron experiences Coulomb attraction toward a nucleus with two positive charges, and mutual repulsion between the electrons must also be considered [22]:

$$H = \sum_{i=1}^{2} \left(\frac{\hbar^2}{2\mu} \nabla_i^2 - \frac{q_\mathrm{e}^2}{4\pi\epsilon_0} \frac{2}{r_i} \right) + \frac{q_e^2}{4\pi\epsilon_0} \frac{1}{|r_1 - r_2|}, \tag{2.27}$$

where the indices i refer to the electron on which the operator acts. This Hamiltonian describes both electrons in optically active states. In this notation, the electrons cannot be distinguished. However, if one electron is in a cRy state while the other remains close to the ground state, they can be distinguished [23]. Rewriting the Hamiltonian, where $i = 1$ denotes the ground state electron and $i = 2$ denotes the Rydberg electron, gives:

$$\begin{aligned} H &= \left(-\frac{\nabla_1^2}{2} - \frac{2}{r_1} \right) + \left(-\frac{\nabla_2^2}{2} - \frac{1}{r_2} \right) + \left(\frac{1}{|r_1 - r_2|} - \frac{1}{r_2} \right) && (2.28) \\ &= H_1 + H_2 + H_\mathrm{int}. && (2.29) \end{aligned}$$

To simplify notation, we use atomic units and omit the prefactors $\frac{\hbar^2}{2\mu}$ and $\frac{2q_e^2}{4\pi\epsilon_0}$ in the above equation. The first two terms, H_1 and H_2, describe an electron in the potential of a nucleus with $Z = 2$ and $Z = 1$, respectively. H_int describes the screened electron interaction. Since one electron is near the nucleus and the other is in a cRy state, we can write $r_2 \gg r_1$, and thus the interaction term can be approximated as [24]:

$$\begin{aligned} H_\mathrm{int} &= 4\pi \sum_{a=0}^{\infty} \sum_{b=-a}^{a} \frac{r_1^a}{r_2^{a+1}} \frac{1}{2a+1} Y_{ab}^*(\theta_1, \phi_1) Y_{ab}(\theta_2, \phi_2) - \frac{1}{r_2} && (2.30) \\ &= 4\pi \sum_{a=1}^{\infty} \sum_{b=-a}^{a} \frac{r_1^a}{r_2^{a+1}} \frac{1}{2a+1} Y_{ab}^*(\theta_1, \phi_1) Y_{ab}(\theta_2, \phi_2). && (2.31) \end{aligned}$$

From this notation, we see that to order $a = 0$, the interaction vanishes. For higher orders, the term $\frac{r_1^a}{r_2^{a+1}}$ becomes very small. Thus, to first order, we can distinguish the two electrons and treat them as independent. This enables us to write the electron wave function as a product:

$$\psi_{1,2}(\mathbf{r}) \approx \psi_1(\mathbf{r})\psi_2(\mathbf{r}). \tag{2.32}$$

This means that the wave function is separable, and we can treat the two electrons independently. Therefore, when calculating transition elements between two Rydberg states, we do not need to account for the inner valence electron. In the limit of vanishing electron-electron interaction, the cRy states of an alkaline-earth atom can therefore be treated in the framework of circular states of alkali atoms discussed in Sec. 2.3.1.

2.4 Circular Rydberg states in external electric field

The Coulomb potential in the Hamiltonian description of hydrogen, as seen in Eq. 2.1, results in a degeneracy of the eigenenergy with respect to l and m_l. Consequently, the corresponding eigenstates are prone to instability due to coupling with stray fields. To mitigate this instability, we examine the effect of a constant electric field, which introduces a Stark shift. This analysis follows the methodology presented in the PhD thesis of Thanh-Long Nguyen. For a more comprehensive discussion, please refer to [20].

We will consider an electric field $\mathbf{F} = F\hat{\mathbf{z}}$ along the $\hat{\mathbf{z}}$ direction, such that the modified Coulomb potential reads:

$$V_\mathrm{S}(r) = -\frac{1}{r} + \mathbf{F}z. \tag{2.33}$$

The introduction of the electric field breaks the spherical symmetry of the potential. Solving the Hamiltonian with the modified potential V_S for eigenstates requires a change to the parabolic basis. The new solutions are quantized by n, m_l, and the new quantum numbers n_1 and n_2, defined by [20]:

$$n = n_1 + n_2 + |m| + 1, \tag{2.34}$$

$$k = n_2 - n_1 = n - 2n_1 - |m| - 1. \tag{2.35}$$

The perturbation of energy can be expanded in powers of the electric field and reads:

$$E_{n,k,m_l} = E^{(0)}_{n,k,m_l} + E^{(1)}_{n,k,m_l} + E^{(2)}_{n,k,m_l} + \cdots \tag{2.36}$$

where the first three orders are given by [20]:

$$E^{(0)} = -\frac{1}{2n^2}, \tag{2.37}$$

$$E^{(1)} = \frac{3}{2}knF, \tag{2.38}$$

$$E^{(2)} = -\frac{1}{16}\left[17n^2 - 9m^2 + 19 - 3k^2\right] n^4F^2. \tag{2.39}$$

For the state $|50C\rangle$, the correction shifts the energy by approximately $2\,\mathrm{MHz}\left(\frac{\mathrm{cm}}{\mathrm{V}}\right)^2$. As discussed in the previous section, this effect surpasses the fine structure, allowing us to neglect fine structure

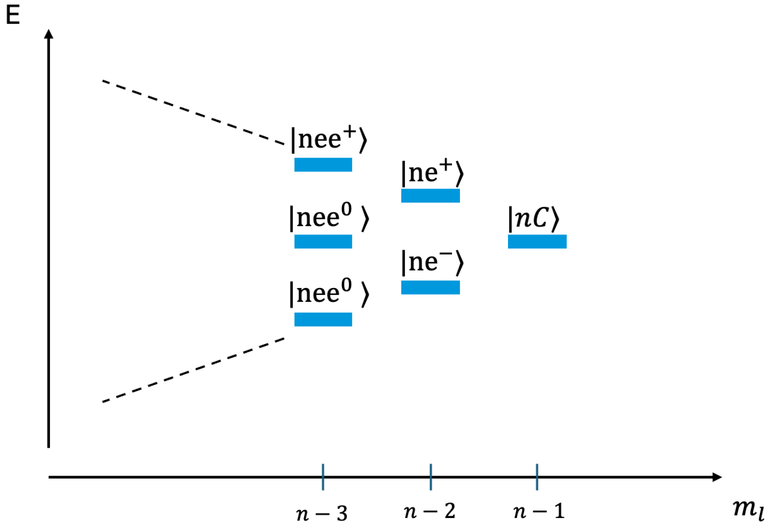

Figure 2.3: Stark map showing the energy splitting of previously degenerate states of high orbital momentum l due to the presence of an external electric field $\mathbf{F} = F\hat{\mathbf{z}}$. The non-circular states are called elliptical states. This figure is adopted from the PhD thesis of Thanh-Long Nguyen [20].

corrections. However, for the purposes of this thesis, we can also disregard this shift since it is small compared to the energy difference between two circular states with adjacent n. The energy difference between two adjacent Stark manifolds, i.e., manifolds with different principal quantum numbers n, is on the order of GHz, see Eq. 2.9. Therefore, a shift on the order of MHz results in a wavelength shift for a photon on the order of a tenth of a percent. The energy splitting due to the modified potential in Eq. 2.33 is schematically illustrated in Fig. 2.3. For each value of n, one speaks about a Stark manifold. In addition to the circular state, there are the elliptical states, which are either symmetric or anti-symmetric combinations of states in the n, l, m_l basis [20]:

$$\begin{aligned} |ne^+\rangle &= |n, k = +1, m = n-2\rangle \\ &= \frac{1}{\sqrt{2}} \left(|n, l = n-2, m_l = n-2\rangle + |n, l = n-1, m_l = n-2\rangle \right), \end{aligned} \tag{2.40}$$

$$\begin{aligned} |ne^-\rangle &= |n, k = -1, m_l = n-2\rangle \\ &= \frac{1}{\sqrt{2}} \left(|n, l = n-2, m = n-2\rangle - |n, l = n-1, m_l = n-2\rangle \right). \end{aligned} \tag{2.41}$$

2.5 Calculation of lifetime for circular Rydberg states in free space

The lifetime of cRy states is exceptionally long for highly excited atoms. This extended lifetime can be explained quantum mechanically by the fact that cRy atoms possess maximal angular momentum. They can only decay by reducing the magnetic quantum number m_l through a microwave transition from $|nC\rangle$ to $|(n-1)C\rangle$. In contrast, low-angular momentum Rydberg states have numerous allowed decay transitions in the optical domain. The transition rates, which are proportional to the cube of the transition frequency, partially account for the comparatively long lifetime of the circular states. Deriving the lifetimes of cRy states will be divided into two parts.

In the first part, we will derive the decay mechanisms of atoms in free space using Fermi's golden rule. Therefore, we will derive the dipole Hamiltonian starting from the general form of the Hamiltonian coupling light to matter. From this, we find the dominant decay terms to be the dipole transitions and examine the coupled states. To this end, we are then able to identify possible decay channels and derive an expression for the total rate of depopulation of any initial state. In the second part, the resulting lifetime in free space of the state $|50C\rangle$ of the atom ^{40}Ca. An outline on the implementation in python is given. The results are analyzed, and scaling laws in terms of the principal quantum number n are derived for low and high-temperature limits. With this, we conclude the chapter on lifetimes in free space and turn our attention to the lifetimes of cRy states in spontaneous inhibitors.

2.5.1 Fermi's golden rule

The transition rate between an initial state $|i\rangle$ and a final state $|f\rangle$ can be calculated using Fermi's golden rule [21]:

$$\Gamma = \frac{2\pi}{\hbar^2} \sum_{i,f} \left|\langle f|H_I|i\rangle\right|^2 \rho(\omega_{if}). \tag{2.42}$$

Here, H_I denotes the interaction Hamiltonian coupling the two states, and $\rho(E_{if})$ is the density of photonic states with the respective energy $\omega_{if} = \frac{|E_f - E_i|}{\hbar}$. H_I for light-matter interaction reads [25]:

$$H_I = \frac{1}{2m}(\mathbf{p} - q_\mathrm{e}\mathbf{A})^2 + q_\mathrm{e}\phi. \tag{2.43}$$

Here, $\mathbf{p}$ is the momentum operator of the electron, and $\mathbf{A}$ and ϕ are the vector and scalar potentials of the electric field, respectively. For our purpose, we will employ the Coulomb gauge $\nabla \cdot \mathbf{A} = 0$, the radiation gauge $\phi = 0$, and operate in the dipole approximation (uniform field over the size of the atom). The interaction Hamiltonian then reads:

$$H_I \simeq -\mathbf{d} \cdot \mathbf{E}(\mathbf{r}, t). \tag{2.44}$$

This approximation leads us to consider only the most dominant interaction, which is due to the coupling of the dipole moment $\mathbf{d}$ to the electric field $\mathbf{E}$. Only two states where the quantum numbers fulfill the selection rules [25]:

$$|l_f - l_i| = 1, \tag{2.45}$$

$$m_{l_i} + q = m_{l_f}, \tag{2.46}$$

can be coupled. The transition is said to be π-polarized for $q = 0$ and $\sigma^\pm$ for $q = \pm 1$. Other states are not coupled with the Hamiltonian in Eq. 2.44.

In a semi-classical picture, we consider an electric field with amplitude E_0 pointing in some direction

$\mathbf{z}$ to be defined as [25]:

$$\begin{aligned}\mathbf{E}(t) &= E_0 \cos(\omega t)\hat{\mathbf{z}} \qquad (2.47)\\ &= \left(\frac{\hbar\omega}{2\epsilon_0 V}\right)^{0.5} \cos(\omega t)\hat{\mathbf{z}}, \qquad (2.48)\end{aligned}$$

where ω is the frequency of the electric field and V describes the volume of interest. Furthermore, the density of modes inside a volume V can be derived by considering the number of modes that can fit into a cubic box [26]:

$$\rho(\omega) = \frac{V\omega^2}{\pi^2 c^3}. \tag{2.49}$$

First, we want to discuss the spontaneous decay. Let us consider an atom in the initial state $|i\rangle$ placed in an environment at zero temperature. The initial electronic state can only decay by emitting a photon with the frequency $\omega_{if} = \frac{|E_i - E_f|}{\hbar}$ into an energetically lower state $|f\rangle$. $E_{i,f}$ here denotes the energy of the respective state. The decay rate reads:

$$\Gamma^{\text{spont}}_{i\to f} = \frac{4\alpha\omega_{if}^3}{3c^2} \left|\langle i|\mathbf{r}|f\rangle\right|^2, \tag{2.50}$$

where c is the velocity of light in vacuum.

In the case where the environment of the atom has a non-zero temperature, field modes can be populated with thermal photons. The presence of black-body radiation introduces two decay processes stimulated by a thermal photon on the atom. Their rate increases linearly with the number of photons that are resonant with the transition frequency. The stimulated decay rates, as opposed to the spontaneous decay, are multiplied by the mean number of photons inside a mode of frequency ω at a given temperature T. This number is given by [25]:

$$n_{\text{th}}(\omega, T) = 1/(e^{\hbar\omega/k_{\text{B}}T} - 1). \tag{2.51}$$

Here $\hbar = h/2\pi$ is the reduced Planck constant and k_B is the Boltzmann constant.

For one, an atom in state $|i\rangle$ could absorb a photon resonant with the transition to some energetically higher-lying state $|f'\rangle$. The rate describing the absorption of a photon can be written as:

$$\Gamma^{\text{abs}}_{i\to f'} = \frac{4\alpha\omega_{if'}^3}{3c^2} \left|\langle i|\mathbf{r}|f'\rangle\right|^2 \, n_{\text{th}}(\omega_{if'}, T). \tag{2.52}$$

On the other hand, a photon incident on an excited state could trigger a stimulated emission into its mode, if the resonance condition between the higher-lying state $|i\rangle$ and the lower-lying state $|f\rangle$ is fulfilled. The transition rate for stimulated emission is calculated to be:

$$\Gamma^{\text{stim}}_{i\to f} = \frac{4\alpha\omega_{if}^3}{3c^2} \left|\langle i|\mathbf{r}|f\rangle\right|^2 \, n_{\text{th}}(\omega_{if}, T). \tag{2.53}$$

To consider the total rate of depopulation of the initial state $|i\rangle$, we thus need to sum up all rates from the initial state $|i\rangle$ to every possible final state $|f\rangle, |f'\rangle$:

$$\Gamma_i = \sum_{f<i} \left(\Gamma^{\text{spont}}_{i \to f} + \Gamma^{\text{stim}}_{i \to f} \right) + \sum_{f'>i} \Gamma^{\text{abs}}_{i \to f'}. \tag{2.54}$$

In the subscript of the sum in Eq. 2.54, $<$ and $>$ denote the relation of the energy of the initial and final state. Finally, we want to point out that the decay rates scale with the cube of the transition frequency. As we will see in the following section, the transition frequency of the discussed decay channels is quite large. This leads to comparatively high decay rates, emphasizing the need for inhibition.

2.5.2 Result

Here, we discuss the lifetime of the $|50C\rangle$ state of ^{40}Ca. Figure 2.4 illustrates the light-atom interactions that contribute to the decay processes described in Eq. 2.54. Transitions arising from the definition of elliptical states, see Eq. 2.41, and the dipole selection rules, see Eq. 2.46, are considered. For the calculation of the spontaneous and stimulated emission as well as the absorption, see Eq. 2.50, 2.53, and 2.52, the transition frequency ω_{if}, the transition matrix element $\langle i|\mathbf{r}|f\rangle$, and the number of resonant photons due to black-body radiation n_{th} need to be calculated. While an expression has been derived to calculate the number of resonant photons, see Eq. 2.51, an approximation of the transition frequency derived for hydrogen and the calculation of the transition matrix element will be discussed.

When looking at the transition frequency resulting from hydrogen in Eq. 2.9 for states with large principal quantum number n we might approximate to

$$\omega_{n,n-1} \simeq 2 \frac{\text{Ry}}{h} \frac{1}{n^3}. \tag{2.55}$$

For the purpose of this work here we will neglect the shift in frequency resulting from the external electric field discussed in Sec. 2.4.

The transitional matrix element using the n, l, m_l-basis to describe the states is defined as:

$$\langle n_i, l_i, m_{l_i} |\mathbf{r}| n_f, l_f, m_{l_f} \rangle = (-1)^{l_i - m_{l_i}} \begin{pmatrix} l_i & 1 & l_f \\ -m_{l_i} & q & m_{l_f} \end{pmatrix} \langle l_i |\mathbf{r}| l_f \rangle, \tag{2.56}$$

where $q = m_{l_f} - m_{l_i}$ describes the polarization of the photon connected to the transition, and the term on the right-hand side in round brackets is the Wigner-3j symbol. The last term on the right-hand side is the reduced matrix element and reads:

$$\langle l_i |\mathbf{r}| l_f \rangle = (-1)^{l_i} \sqrt{(2l_i + 1)(2l_f + 1)} \begin{pmatrix} l_i & 1 & l_f \\ 0 & 0 & 0 \end{pmatrix} \int R_{n_i,l_i}(r) r R_{n_f,l_f}(r) r^2 \, dr. \tag{2.57}$$

Here $R_{n,l}(r)$ denotes the radial wave function which was derived for hydrogen in the second line of Eq. 2.3. Using the above calculation, the dipole moments shown in Fig. 2.4 are obtained using the formula:

$$|d_q|^2 = q_{\text{e}}^2 \left| \langle n_i, l_i, m_{l_i} |\mathbf{r}| n_f, l_f, m_{l_f} \rangle \right|^2, \tag{2.58}$$

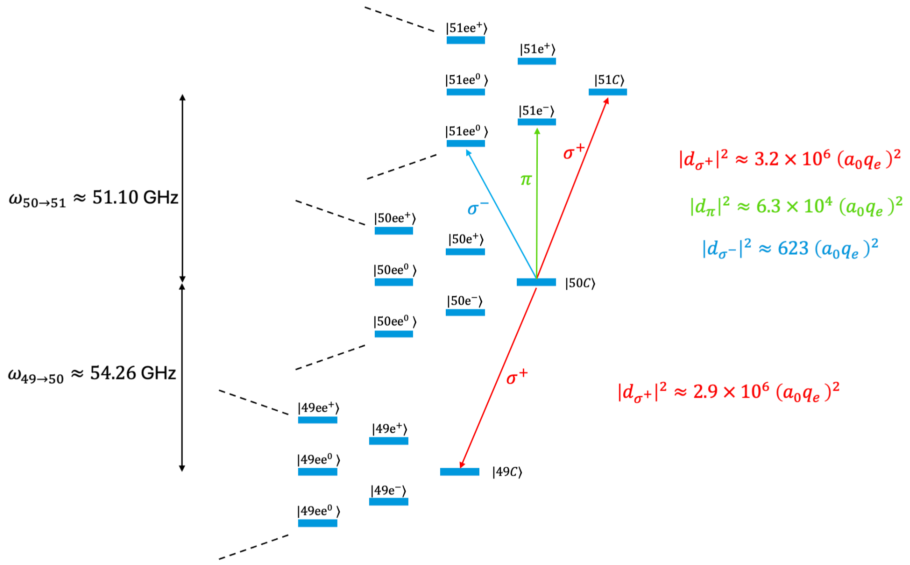

Figure 2.4: Dipole transitions contributing to the decay of the $|50C\rangle$ state of ^{40}Ca. The figure shows $\sigma^\pm$ and π decays and their respective strengths in terms of the dipole moment. The energy difference between states with different n is on the order of GHz.

where $q = m_{l_f} - m_{l_i}$ denotes the polarization of the transition. Circular polarization $\sigma^\pm$ corresponds to $q = \pm 1$, and linear polarization π corresponds to $q = 0$. In Fig. 2.4 the magnitude of the dipole moments behaves as $|d_{\sigma^+}| \gg |d_\pi| \gg |d_{\sigma^-}|$. Therefore, the atom is most likely to decay via the emission or absorption of a σ^+-polarized photon if the polarization of the electric field is uniform. It is important to note that a circular state can decay through only four channels. Three decay channels (σ^+, σ^-, and π-polarized) lead to energetically higher-lying states and are thus related to the absorption of a photon. Only a single σ^+-polarized decay channel leads to an energetically lower-lying state, which is again a circular state. This decay channel is associated with spontaneous and stimulated decay and is the only active decay channel in a zero-temperature environment.

Figure 2.5 shows the lifetime (on a logarithmic scale) of circular Rydberg states as a function of the principal quantum number for different temperatures. The lifetimes are computed for different temperatures, with the solid lines serving as guides to the eye, according to Eq. 2.54. At cryogenic temperatures circular Rydberg states are approximately 100 times more long lived than at room temperature, highlighting the need to inhibit black-body induced decay for circular Rydberg states. Furthermore, in Fig. 2.5, one can observe increasing slopes for lower temperatures. While the slopes for temperatures $T = 100$ and 300K are similar, the slopes for $T = 0.1$K, $T = 1$K, and $T = 2$K are different. The change in slope can be attributed to the impact of black-body induced decay. At $T = 0.1$K, thermal excitations of the field can be neglected, and spontaneous decay dominates. For intermediate temperatures, such as $T = 1$ and 2K, stimulated decay becomes significant but does not dominate the decay process. At higher temperatures, such as $T = 100$ and 300K, black-body induced decay is the predominant effect.

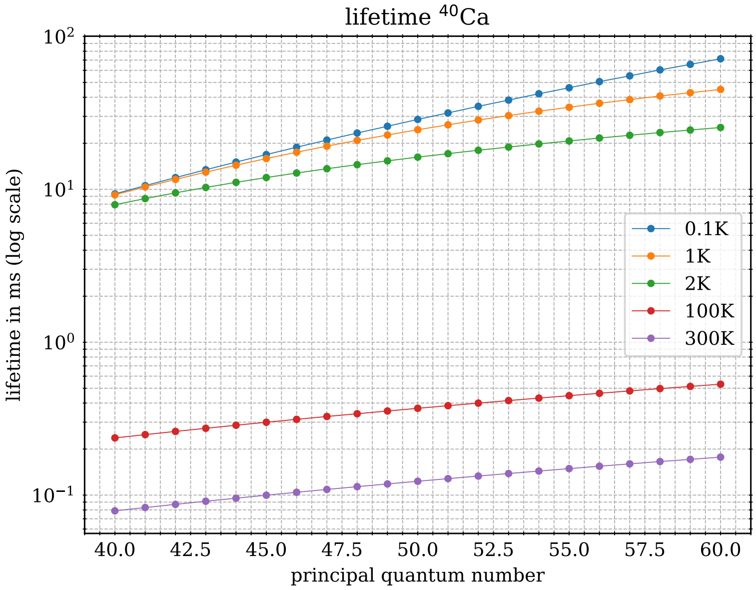

Figure 2.5: Calculated lifetime of the $|50C\rangle$ state of ^{40}Ca for different temperatures $T = 0.1, 1, 2, 100, 300$K. The different slopes for different temperatures indicate the strong dependence of lifetime on stimulated decay induced by black-body radiation.

2.6 Lifetime scaling with n for circular Rydberg states

For the different behaviors attributed to temperature in Fig. 2.5, one can derive scaling laws in terms of n. In the low-temperature limit ($T \approx 0$), almost no thermal photons are excited, and thus the state decays mainly via spontaneous emission. The radiative lifetime of the state can be obtained by equating two expressions for the radiated power. On the one hand, the radiated power of the state is just the dissipated energy, given by the emitted photon $E_{\mathrm{ph}} = hf$ divided by the lifetime:

$$P_r = \frac{hf_{if}}{\tau_i}. \tag{2.59}$$

On the other hand, for accelerated charged particles, the Larmor formula predicts a radiated power of [21]:

$$P_r = \frac{q_{\mathrm{e}}^2 a^2}{6\pi\epsilon_0 c^3}. \tag{2.60}$$

The modulus of the acceleration $a = |\mathbf{a}|$ of the electron in its circular orbit can be derived by considering the Coulomb force F_C acting on the electron. Solving for the acceleration yields:

$$a = \frac{F_C}{m_{\mathrm{e}}} \tag{2.61}$$

$$= \frac{1}{m_{\mathrm{e}}} \frac{q_{\mathrm{e}}^2}{4\pi\epsilon_0 (a_0 n^2)^2}. \tag{2.62}$$

For the distance between the electron and the core, we used Eq. 2.23. Now, by substituting the photon frequency f_{if} from the expression in Eq. 2.55 and solving for $\Gamma_i = \frac{1}{\tau_i}$, we obtain:

$$\Gamma_n = \frac{4}{3}\frac{R_y}{\hbar}\alpha^3 n^{-5}, \tag{2.63}$$

which exhibits the remarkable dependence of n^{-5} in the absence of thermal photons leading to the favorable long lifetimes.

For higher temperatures, the effects of black-body radiation need to be taken into account. In the presence of a thermal field with n_{th} photons per mode on average, the decay rate can be approximated by multiplying the above equation by $1 + n_{\text{th}}$ [21]. For high temperatures T, the mode population due to thermal excitation can be approximated as $n_{\text{th}} \propto \frac{k_B T}{\hbar\omega}$. Using the relation between the transition frequency and the principal quantum number (see Eq. 2.55), for the high-temperature limit we obtain:

$$\Gamma_n \simeq \frac{4}{3}\frac{k_B \alpha^3}{\hbar^2} n^{-2} T. \tag{2.64}$$

We obtain the result that, in cases where stimulated decay processes can be neglected, the lifetime scales with $\tau_i \propto n^5$, while for temperatures where many photons are excited in the modes, the stimulated decay processes dominate and the lifetime scales less strongly with the principal quantum number $\tau_i \propto n^2 T$. This result is in agreement with the observations from Fig. 2.5 of the lifetimes of $|50C\rangle$ of ^{40}Ca. As the slope visibly decreases, we can assume that for temperatures of $T \approx 1$K, black-body induced decay is no longer negligible.

Chapter 3

Inhibition of spontaneous decay

3.1 Method 1

When examining the decay rates in Sec. 2.5, we observe that the term coupling the initial and final states in Fermi's golden rule can be approximated by the dipole Hamiltonian, as shown in the derivation of Eq. 2.44. The dipole Hamiltonian consists of the product of the dipole operator and the electric field. Therefore, a change in the electric field amplitude also induces a change in the respective decay rates summarized in Eq. 2.54. We aim to investigate the effect that the presence of two conducting plates has on the electric field compared to free space and, consequently, on the coupling strength towards a cRy state between them. The idea is to write down the electric field solution for both cases. This can be done by using Maxwell's equation and solving for appropriate boundary conditions. From this, one should obtain a steady-state solution of the electric field inside the closed system of the conducting plates. Then, one can equate the energy stored in the electric field mode with the energy of a photon with the same frequency. In this way, it is possible to obtain the electric field amplitude for both cases and express the field amplitude between the conducting plates in terms of the free space amplitude. As the square of the electric field amplitudes enters Eq. 2.54, the ratio of the square of the amplitudes just gives the ratio between the decay rate in free space and between the conducting plates. Fig. 3.1 shows, in cylindrical coordinates, the envisioned system of a cRy state between two conducting plates separated by a distance z.

This procedure works for the case where perfectly conducting plates are assumed. The infinite conductivity leads to zero field amplitudes inside the conductors. Therefore, the energy of the field is not dissipated but is conserved in the electromagnetic waves between the conducting plates. The solution to this problem has not been outlined here due to constraints of time, but an excellent discussion can be found in 'The Quantum Theory of Light' by Rodney Loudon [27].

However, if imperfect conductors are assumed, this is not the case anymore. In this case, the electric field penetrates into the conductors and, therefore, the energy of the electric field also needs to be taken into account. When an electric field exists inside a conductor, it interacts with charged particles, i.e., it exerts a force on the electrons. These electrons may collide with positively charged nuclei or they collide with each other, resulting in energy dissipation due to phononic excitations. These processes are not accounted for by the description of Maxwell's equations and boundary conditions used for the case of perfect conductors. Therefore, the system under investigation is not closed and further effects need to be taken into consideration for the system to have a steady-

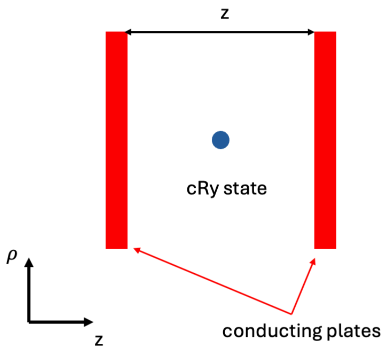

Figure 3.1: Scheme of a circular Rydberg state at the center between two conducting plates, which are separated by a distance z. The system is oriented in cylindrical coordinates such that the surface of the conducting plates is normal to the unit vector $\hat{\mathbf{z}}$.

state solution. Consequently, we haven't completed the method, as we realized that in the way we outlined it, it can only work for perfect conductors.

3.2 Method 2

The concept behind this method is to compare the radiated power of an atom in free space with its radiated power when positioned between two conducting plates. We model the atom as an oscillating dipole antenna. Using the equation of the electric field, we can determine the radiated power through the Poynting vector. When conducting plates are present, the electric field is altered. To calculate the modified electric field, we use the method of images, which calculates the electric field at the atom's location as a superposition of electric fields from infinetly many dipole antennas. The positions and orientations of these antennas are derived using the method of images.

This discussion is divided into three parts: an overview of the method of images for this specific case, perfectly conducting plates, and imperfectly conducting plates. The latter represents the practical situation of lossy conductors with finite conductivity. To model the losses in the imperfect conductor, we introduce a reflectivity $r < 1$ and a phase retardation ϕ upon reflection. By comparing the results from both types of plates, we aim to understand how finite conductivity affects the inhibition factor.

3.2.1 Method of images

A common method to solve problems in electrostatics is the method of mirror charges. Under favorable conditions, it can be inferred from the given geometry that a small number of charges, suitably placed outside the region of interest, can simulate the required boundary conditions of the original situation. These charges are called image charges. Thus, the actual boundary value problem is replaced by an equivalent problem with an extended domain that includes mirror charges.

In our case, we model the atom as a dipole antenna placed at the origin, in the center of two conducting plates separated by a distance z. The symmetry of the problem allows us to use cylindrical coordinates. We align the surface of the plates to be perpendicular to the $\hat{\mathbf{z}}$-axis. Therefore, we can separate the electric field into a parallel component $\mathbf{E}_\rho$ and a perpendicular component $\mathbf{E}_z$ relative to the surface of the plates, as shown in Fig. 3.2. We define the quantization axis along $\hat{\mathbf{z}}$. This definition allows us to associate the discussed π transitions with a field polarized along $\mathbf{E}_z$, while the $\sigma^\pm$ decay channels are driven by the parallel field component $\mathbf{E}_\rho$.

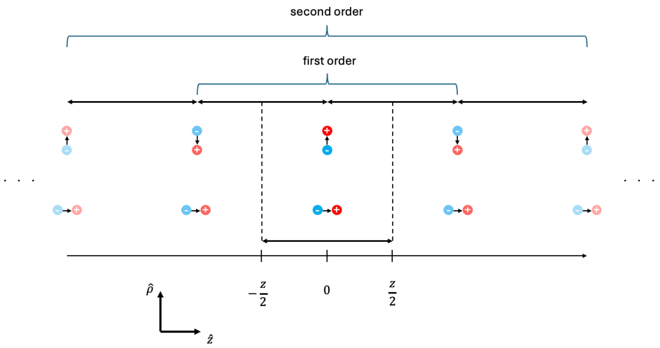

Figure 3.2: Schematic drawing of the parallel (upper) and the perpendicular (lower) orientation of the dipole with respect to the surface of the conducting plates. The dipole modeling the atom is positioned at the origin $z = 0$, while the mirror charges are grouped by order and have pairwise matching opacity. The dots on the right and left sides indicate the infinite sequence of mirror charges. The positions of the conducting plates at $\pm\frac{z}{2}$ are denoted with a dashed line.

Fig. 3.2 shows the method of images for cases where a dipole points along the $\hat{\rho}$ and $\hat{\mathbf{z}}$ directions. The two alignments of the dipole in the figure should be considered as distinct cases of alignment and are treated separately. The dashed line indicates the original boundary conditions given by the conducting plates in the actual setup. The dipoles appear equidistant, matching the spacing of the conducting plates. The first-order mirror charges, at a distance z from the origin, arise from mirroring the original dipole at the origin at the plane of the conducting plates. The second-order mirror charges, at a distance $2z$ from the origin, arise due to reflections of the first-order mirror charges at the plane of the conducting plates, and so on. This leads to an infinite series, indicated by the dots on either side of Fig. 3.2. The dipoles on the left/right of order n arise due to a reflection of the mirror dipole of order $n-1$ on the right/left side mirrored at the right/left conducting plate. For a dipole parallel to the surface, the image dipole orientation is switched with each reflection, whereas for the perpendicular polarization, the alignment remains the same. Thus, we can write the dipole moment of a mirror charge at a distance nz away from the origin as:

$$\mathbf{d}_n = \begin{pmatrix} (-1)^n d_\rho \\ 0 \\ d_z \end{pmatrix} \tag{3.1}$$

3.2.2 Perfect conductor

First, the electric field of a dipole antenna in free space is introduced. Using the Poynting vector, the radiated power in free space can be immediately obtained. From this, we derive the total electric field at the center point, considering the field generated by the mirror charges. The treatment will be divided into the electric field components parallel $\mathbf{E}_\rho$ and perpendicular $\mathbf{E}_z$ to the surface of the conducting plates.

An external electric field along the $\hat{\mathbf{z}}$-direction defines the quantization axis and thus aligns the cRy states perpendicular to the surface of the conductors. Therefore, the parallel and perpendicular electric fields give rise to $\sigma^{\pm}$- and π-decay, respectively. For the atom between two conductors, an equivalent method of calculating the radiated power is outlined. Ultimately, an expression for the inhibited decay rates, depending on the polarization of the electric field, is derived, and its function is plotted and analyzed.

Electric field due to mirror charges

Having discussed the setup of mirror charges, we start by writing down the electric field of a dipole antenna with frequency ω and wave number $k = |\mathbf{k}|$ as [28]:

$$\boldsymbol{E}(\boldsymbol{r},t) = \frac{k^3 e^{ikr}}{4\pi\varepsilon_0}\left\{(\hat{r}\times\boldsymbol{d})\times\hat{r}\left(\frac{1}{kr}\right) + [3\hat{r}(\hat{r}\cdot\boldsymbol{d}) - \boldsymbol{d}]\left(\frac{1}{(kr)^3} - \frac{i}{(kr)^2}\right)\right\}e^{i\omega t}. \tag{3.2}$$

The orientation of the dipole is given by the vector $\boldsymbol{d}$, while the unit vector $\boldsymbol{r}$ points from the dipole to the position in space where we want to calculate the field, in this case, the origin. Furthermore, ω denotes the frequency of the electric field.

Now we want to investigate the modification of the electric field inside two conducting plates. The electric field of a charge positioned at $\pm\boldsymbol{r}_n = \pm nz\hat{\boldsymbol{z}}$ relative to the origin using Eq. 3.2 reads:

$$\begin{aligned}\boldsymbol{E}_n(\pm\boldsymbol{r}_n,t) = \frac{k^3 e^{\pm iknz}}{4\pi\varepsilon_0}&\left\{(-1)^n d_\rho\,\hat{\boldsymbol{\rho}}\left(\frac{1}{\pm knz} + \frac{i}{(\pm knz)^2} - \frac{1}{(\pm knz)^3}\right)\right.\\ &\left.+2d_z\,\hat{\boldsymbol{z}}\left(\frac{1}{(\pm knz)^3} - \frac{i}{(\pm knz)^2}\right)\right\}e^{i\omega t}. \end{aligned}\tag{3.3}$$

As shown in Fig. 3.2, we will treat mirror charges with the same absolute distance to the origin together by superposing their electric field components. For the analysis, we will treat the field with parallel $E_\rho = \hat{\boldsymbol{\rho}}\boldsymbol{E}$ and perpendicular $E_z = \hat{\boldsymbol{z}}\boldsymbol{E}$ polarization separately. By summing the contributions of the two charges at distance nz from the origin, we obtain:

$$\hat{\boldsymbol{\rho}}\cdot(\mathbf{E}_n(\mathbf{r}_n,t) + \mathbf{E}_n(-\mathbf{r}_n,t)) = \frac{ie^{i\omega t}k^3 d_\rho}{2\pi\epsilon_0}(-1)^n\left\{\frac{\sin\phi_n}{\phi_n} + \frac{\cos\phi_n}{\phi_n^2} - \frac{\sin\phi_n}{\phi_n^3}\right\} \tag{3.4}$$

$$\hat{\mathbf{z}}\cdot(\mathbf{E}_n(\mathbf{r}_n,t) + \mathbf{E}_n(-\mathbf{r}_n,t)) = \frac{ie^{i\omega t}k^3 d_z}{\pi\epsilon_0}\left\{-\frac{\cos\phi_n}{\phi_n^2} + \frac{\sin\phi_n}{\phi_n^3}\right\}. \tag{3.5}$$

For more compact notation, we substitute $\phi_n = knz$ in the above equations. We calculate the total electric field at the origin due to the original dipole and the mirror charges as $\mathbf{E}_{\text{tot},i} = \sum_n \hat{\mathbf{i}}\cdot(\mathbf{E}_n(\mathbf{r}_n,t) + \mathbf{E}_n(-\mathbf{r}_n,t))$ and therefore get:

$$\mathbf{E}_{\text{tot},\rho} = \frac{ie^{i\omega t}k^3 d_\rho}{2\pi\epsilon_0}\sum_n(-1)^n\left\{\frac{\sin\phi_n}{\phi_n} + \frac{\cos\phi_n}{\phi_n^2} - \frac{\sin\phi_n}{\phi_n^3}\right\} \tag{3.6}$$

$$\mathbf{E}_{\text{tot},z} = \frac{ie^{i\omega t}k^3 d_z}{\pi\epsilon_0}\sum_n\left\{-\frac{\cos\phi_n}{\phi_n^2} + \frac{\sin\phi_n}{\phi_n^3}\right\}. \tag{3.7}$$

Factor of spontaneous inhibition

The above equations describe the electric field at the origin due to the presence of infinitely many mirror dipoles assembled as indicated in Fig. 3.2. Ultimately, we want to calculate the change in decay rate due to the presence of the conducting plates. However, the rate of decay is just the radiated power of the dipole [28]. We will develop the necessary formula starting from the well-known Poynting vector [29]:

$$\mathbf{Q} = \mathbf{E} \times \mathbf{H}, \tag{3.8}$$

which describes the energy flux density due to electromagnetic waves. Here, $\mathbf{E}$ and $\mathbf{H}$ describe the electric and magnetic fields of the dipole, respectively. Poynting's theorem tells us that the radiated power P corresponds to the time average $\langle \mathbf{Q}(\mathbf{r}) \rangle$ of the energy flux [29]:

$$\langle \mathbf{Q}(\mathbf{r}) \rangle = \frac{1}{2} \mathrm{Re} \left\{ \mathbf{E}(\mathbf{r}) \times \mathbf{H}^*(\mathbf{r}) \right\}, \tag{3.9}$$

through the surface ∂V of a volume that encloses the radiation source. The expression for the radiated power through the surface of a volume thus reads [29]:

$$\begin{align} P &= \int_{\partial V} \langle \mathbf{Q}(\mathbf{r}) \rangle \cdot \mathbf{n} \, da \tag{3.10} \\ &= -\frac{1}{2} \int_{\partial V} \mathrm{Re}\{\mathbf{E}(\mathbf{r}) \times \mathbf{H}^*(\mathbf{r})\} \mathbf{n} \, da. \tag{3.11} \end{align}$$

In Eq. 3.11, $\mathbf{n}$ is a unit vector normal to the surface element da describing ∂V. Given the electric field of a dipole in free space, see Eq. 3.2, we can now calculate its free-space radiated power to be [30]:

$$P_0 = \frac{|\mathbf{d}|^2 k^3 \omega}{12 \pi \varepsilon_0}. \tag{3.12}$$

Next, we want to compare the radiated power for the superposed field of mirror charges, see Eq. 3.7 to the dissipated power in free space. However, it is challenging to calculate the magnetic field $\mathbf{H}$ from the expression of the electric field we derived (Eq. 3.7). There is an easier way to calculate P. For linear, non-dispersive media and fields with harmonic time dependence, using Maxwell's equations, it can be shown that the previously noted form of dissipated power equals [30]:

$$P = -\frac{1}{2} \int_V \mathrm{Re}\{\mathbf{j}^* \cdot \mathbf{E}\} \, dV. \tag{3.13}$$

Here, $\mathbf{j}$ stands for the current density associated with the dipole, and V is the volume enclosing the dipole. We can express the current density in terms of the change of the dipole moment: $\mathbf{j}(\mathbf{r}, t) = \frac{\partial}{\partial t} \mathbf{d}(t) \delta(\mathbf{r} - \mathbf{r}_0)$, where $\mathbf{r}_0$ describes the position of the dipole [30]. If we now consider a dipole moment with harmonic time dependence $\mathbf{d}(t) \propto \mathbf{d} e^{i \omega t}$ and take into account that the δ-function collapses the volume integral, we can rewrite the dissipated power as

$$P = \frac{\omega}{2} \mathrm{Im}\{\mathbf{d}^* \cdot \mathbf{E}_0\} \tag{3.14}$$

Thus the radiated power can be calculated given the expressions for the dipole moment Eq. 3.6 and the superposed electric field Eq. 3.12. We calculate the radiated power for a pair of mirror charges of order n in terms of the free space radiated power P_0 and obtain

$$P_{n,\rho} = 3P_0(-1)^n \left\{ \frac{1}{\phi_n} \sin\phi_n + \frac{1}{\phi_n^2} \cos\phi_n - \frac{1}{\phi_n^3} \sin\phi_n \right\} \tag{3.15}$$

$$P_{n,z} = 6P_0 \left\{ -\frac{1}{\phi_n^2} \cos\phi_n + \frac{1}{\phi_n^3} \sin\phi_n \right\}. \tag{3.16}$$

With this result, we can now obtain the factors of spontaneous inhibition. We do this by first summing the radiated powers of all the dipoles. This includes the dipole antenna modeling the atom at the center as well. After that, we want to normalize by the radiated power of a dipole in free space P_0 to obtain the factors of spontaneous inhibition. We obtain the following results with respect to the polarization

$$\xi_{\sigma^\pm} = 1 + 3\sum_{n=1}^{\infty} (-1)^n \left\{ \frac{1}{\phi_n} \sin\phi_n + \frac{1}{\phi_n^2} \cos\phi_n - \frac{1}{\phi_n^3} \sin\phi_n \right\}, \tag{3.17}$$

$$\xi_\pi = 1 + 6\sum_{n=1}^{\infty} \left\{ -\frac{1}{\phi_n^2} \cos\phi_n + \frac{1}{\phi_n^3} \sin\phi_n \right\}. \tag{3.18}$$

As discussed in Sec. 3.2.1 in the above notation instead of ρ we write $\sigma^\pm$ and instead of z we write π indicating the polarization of the channel being inhibited. This is because the quantization axis in terms of external electric field is applied along $\hat{\mathbf{z}}$-direction leading to the above relations of field polarization and circularly and linearly polarized transitions of the states denoted in Fig. 2.4. In honor of Edward Purcell, who was the first to think about such effects in cavity structures as mentioned in the introduction, the factors $\xi_{\sigma^\pm,\pi}$ are named Purcell factors.

Result

Fig. 3.3 shows the factors of spontaneous inhibition as described in Eq. 3.18 as a function of $\frac{z}{\lambda}$, where z denotes the separation of the conducting plates and $\lambda = \frac{c}{f}$ is the wavelength of the photon. For distances of $z < \frac{\lambda}{2}$, the inhibition factors for both polarizations oscillate between enhancement and inhibition of the decay. For distances of $z > \frac{\lambda}{2}$, the behavior of circularly and linearly polarized light diverges. The $\sigma^\pm$-decay is completely suppressed for separations of the mirrors less than half of the wavelength ($\frac{z}{\lambda} < \frac{1}{2}$). Therefore, no decay shown in Fig. 2.4 involving a circularly polarized photon can occur. This is particularly interesting considering the dominant dipole matrix element, which is attributed to the σ^+ transition for circular states, see Fig. 2.4. However, the transitions via the π-channel are increasingly enhanced with decreasing distance between the conducting plates.

This behavior can be explained by examining the method of images as shown in Fig. 3.2. When the alignment of mirror dipoles alternates in the case of an orientation parallel to the surface of the conductors, decreasing the distance between the plates leads to destructive interference. At short distances, the opposite alignment cancels any electric field. Conversely, when the dipole is aligned normal to the surface of the conducting plate, the mirror charges are aligned. The same line of reasoning in this case leads to constructive interference and thus an increase in the decay rate.

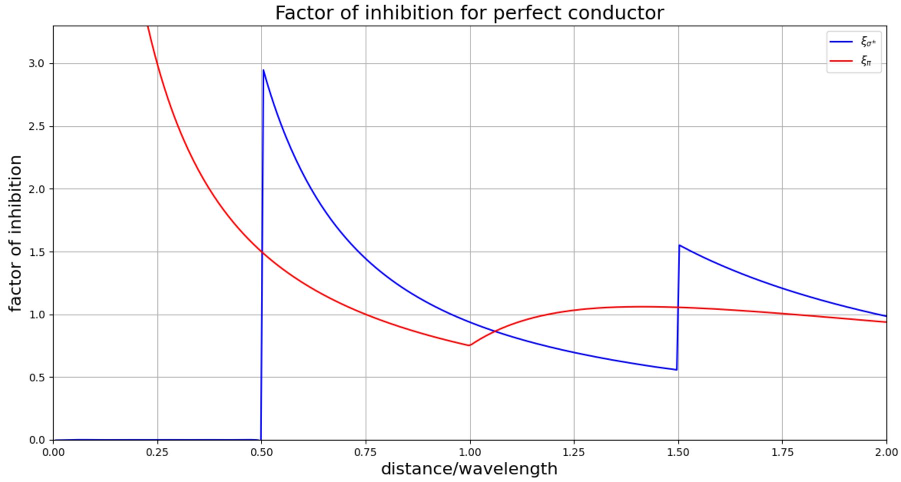

Figure 3.3: Factors of inhibition for $\sigma^{\pm}$- and π-decay for a circular Rydberg state between two conducting plates is shown. The calculation follows Eq. 3.18 It is given as a function of $\frac{z}{\lambda}$, where z is the separation of the conductors and λ denotes the wavelength of the photon. For $\frac{z}{\lambda} > 1/2$ the inhibition factors both oscillate. For $\frac{z}{\lambda} < 1/2$ the $\sigma^{\pm}$-decay is completely inhibited while the π- decay is enhanced.

3.2.3 Imperfect conductor

The above result describes the factor of inhibition for perfect conductors. However, we would like to study the more realistic case of imperfect conductors. For this thesis a non-unity reflectivity r and a retardation phase χ are considered for the conductors. They are introduced upon reflection by multiplication with the electric field of its mirror charge, i.e. the charge it models the boundary condition for. This adds a prefactor of r^n to the field describing a mirror dipole of n^{th} and changes the argument of the trigonometric functions from ϕ_n to $\phi_n + \chi$ in Eq. 3.5. The result is:

$$\xi_{\sigma^\pm} = 1 + 3 \sum_{n=1} (-r)^n \left\{ \frac{1}{\phi_n} \sin\left(\phi_n + \chi\right) + \frac{1}{\phi_n^2} \cos\left(\phi_n + \chi\right) - \frac{1}{\phi_n^3} \sin\left(\phi_n + \chi\right) \right\}, \tag{3.19}$$

$$\xi_{\pi} = 1 + 6 \sum_{n=1} r^n \left\{ -\frac{1}{\phi_n^2} \cos\left(\phi_n + \chi\right) + \frac{1}{\phi_n^3} \sin\left(\phi_n + \chi\right) \right\}. \tag{3.20}$$

The plot of Eq. 3.20 is shown in Fig. 3.4 and Fig. 3.5. The notation of colors is the same as in Fig. 3.3, where blue denotes the inhibition of circular polarization and red the inhibition of linear polarization. For both figures the factors of inhibition are given as a function of $\frac{z}{\lambda}$, where z is the separation of the conducting planes and λ denotes the wavelength at which the inhibition is calculated. In Fig. 3.4 the plots are done for different parameter choices of reflectivity $r = 0.6, 0.9$ and 1 while the phase retardation has been kept constant at $\delta = 0.01$. In Fig. 3.5 The plots are done for different phase retardation factors $\delta = 0, 0.1, 0.01$ and 0.001 while the reflectivity has been kept constant at $r = 0.9$. In contrast to the perfect mirror case, for an imperfect mirror with losses and phase retardation, the decay rate for $\sigma^{\pm}$-decays diverges at small distances between the plates. The behavior for the π-decay is largely similar. As shown in Fig. 3.4, with decreasing reflectivity of the conductors, the features of the factors of inhibition become smoother.

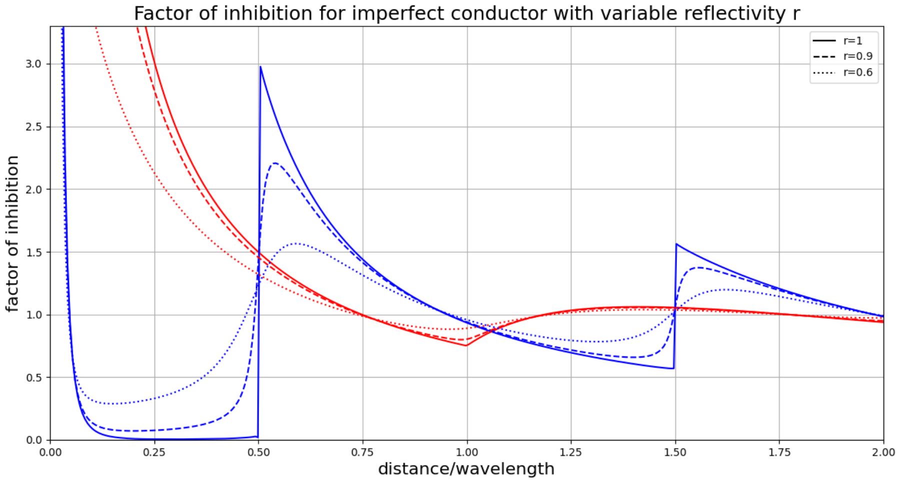

Figure 3.4: Factors of inhibition for mirrors with non-unity reflectivity as calculated in Eq. 3.20. The notation of colors follows Fig. 3.3. The factors are calculated for $r = 0.6, 0.9$ and 1 while the phase retardation has been kept constant at $\chi = 0.01$. Introducing on-unity reflectivity $r < 1$ and a phase difference upon reflection enhance $\sigma^{\pm}$-decay for close distances of the conductors.

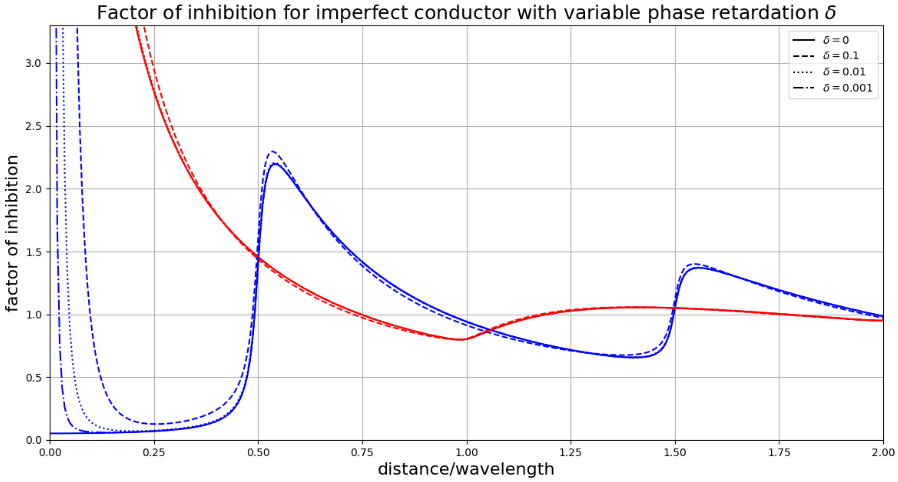

Figure 3.5: Factors of inhibition for mirrors with non-unity reflectivity as calculated in Eq. 3.20. The notation of colors follows Fig. 3.3. The factors are calculated for $\chi = 0, 0.1, 0.01$ and 0.001 with $r = 0.9$. Introducing on-unity reflectivity $r < 1$ and a phase difference upon reflection enhance $\sigma^{\pm}$-decay for close distances of the conductors.

Additionally, increasing the phase retardation leads to the divergence of circularly polarized light at larger separations of the conducting planes, as seen in Fig. 3.5. This divergence is related to the near field of the dipole. In free space, the component of the field out of phase with the dipole tends to a finite value close to the dipole. Near a perfect mirror, the reflection of this field cancels or doubles the decay rate. Conversely, the field in free space that is in phase with the dipole diverges as $1/r^3$. The reflection of this field from a perfect mirror does not modify the decay rate (at least in this first-order perturbation model) due to its phase. However, when the field is reflected with a phase shift from a mirror of finite conductivity, the decay rate diverges near the mirror for both polarizations. This effect can be simply explained physically: the excitation energy of the atom is dissipated through direct Joule heating of the surface by the oscillating Coulomb field of the dipole.

For imperfect mirrors with losses and phase retardation, the decay rate for $\sigma^{\pm}$ decays diverges when the distance between the plates is small, similar to the behavior of π decays. This divergence is linked to the near field of the dipole. In free space, the out-of-phase component of the field reaches a finite value close to the dipole. Near a perfect mirror, the reflection of this field either cancels or doubles the decay rate. On the other hand, the in-phase field component in free space diverges as $1/r^3$. The reflection of this in-phase field from a perfect mirror does not alter the decay rate due to its phase, according to first-order perturbation theory. However, with a mirror of finite conductivity, the decay rate diverges near the mirror for both polarizations because of the phase shift. This effect can be explained by the fact that the atom's excitation energy is dissipated through heating of the mirror's surface by the dipole's oscillating Coulomb field [28].

Chapter 4

Future Work

The first part of this semester project involved familiarizing with the properties of circular Rydberg states. We derived that circular Rydberg states in free space can be approximated by the hydrogen model. However, when exposed to an external electric field, the new eigenstates are defined in the parabolic basis. The respective energy shifts are described by the Stark map. By expressing eigenstates in the parabolic basis through the n, l, m_l-basis, we developed the free space decay rates of a circular Rydberg state using Fermi's golden rule. The calculation of the obtained results exhibited a lifetime increase by a 100-fold at a temperature of $T = 0.1$K compared to room temperature. Furthermore, scaling laws in terms of n for different temperature limits were derived. In the low temperature regime, the decay rates scale as $\Gamma_{i,T_{\text{low}}} \propto n^{-5}$, while in the high temperature regime, the relation is $\Gamma_{i,T_{\text{high}}} \propto n^{-2} T_{\text{high}}$. These scaling laws for the lifetimes match the calculated results from Fermi's golden rule and are responsible for the different slopes in Fig. 2.5.

In the second part, we focused on the modification of the electromagnetic field inside the volume enclosed by a parallel plate capacitor. Our first approach to develop the change in radiated power was not successful. Using the method of mirror charges, we were able to retrieve the factors of inhibition for circular $\xi_{\sigma^\pm}$ and linear ξ_π polarization as a function of spacing between the plates. For plates with infinite conductivity, we observed full inhibition of modes with circular polarization for a separation of $z/\lambda \leq \frac{1}{2}$. However, for π-polarized modes, we saw enhancement for the same distances. These observations align well with the expectations from the method of images. Finally, we added the effect of imperfect mirrors to the discussion by including a non-unity reflection r with variable phase retardation δ upon reflection into the calculation. The comparison of perfect and imperfect conductors yielded that a non-zero phase retardation δ leads to a divergence of the inhibition factor of circularly polarized fields for small spacing of the conducting plates of the capacitor, see Fig. 3.5. Non-unit reflectivities $r < 1$ of imperfect conductors lead to not fully inhibited modes of circular polarization, see Fig. 3.4.

The promising results from this work suggest further research into geometries modifying the density of supported modes in circular Rydberg state settings. On one hand, it seems exciting to investigate the factor of inhibition for other geometries, such as a waveguide instead of two parallel conducting plates [9]. On the other hand, one might obtain very interesting results by exploring different materials used for the inhibition structure and their behavior in the GHz regime [8]. Lastly, we want to mention that for a full analysis, we would need to investigate the effect the spontaneous inhibitor has on the components of the experimental setup, e.g., tweezers trapping the atom.

Furthermore, one could look into the finite size effects of the mirrors, as in this case, they were treated as infinite. Also, the new dominant decay channels can be considered. For example, two-photon processes might become interesting when the dipole transitions discussed in Sec. 2.5 are completely inhibited [16].

Bibliography

[1] A. Osterwalder and F. Merkt. Using high rydberg states as electric field sensors. *Phys. Rev. Lett.*, 82:1831–1834, Mar 1999.

[2] Pascal Scholl, Michael Schuler, Hannah J Williams, Andreas A Eberharter, Daniel Barredo, Kai-Niklas Schymik, Vincent Lienhard, Laura-Phoebe Henry, Timon C Lang, Thierry Lahaye, et al. Quantum simulation of 2d antiferromagnets with hundreds of rydberg atoms. *Nature*, 595(7866):233–238, 2021.

[3] Pascal Scholl, Michael Schuler, Hannah J Williams, Andreas A Eberharter, Daniel Barredo, Kai-Niklas Schymik, Vincent Lienhard, Laura-Phoebe Henry, Timon C Lang, Thierry Lahaye, et al. Quantum simulation of 2d antiferromagnets with hundreds of rydberg atoms. *Nature*, 595(7866):233–238, 2021.

[4] M. Archimi, M. Ceccanti, M. Distefano, L. Di Virgilio, R. Franco, A. Greco, C. Simonelli, E. Arimondo, D. Ciampini, and O. Morsch. Measurements of blackbody-radiation-induced transition rates between high-lying s, p, and d rydberg levels. *Phys. Rev. A*, 105:063104, Jun 2022.

[5] H. Wu, R. Richaud, J.-M. Raimond, M. Brune, and S. Gleyzes. Millisecond-lived circular rydberg atoms in a room-temperature experiment. *Phys. Rev. Lett.*, 130:023202, Jan 2023.

[6] Randall G. Hulet, Eric S. Hilfer, and Daniel Kleppner. Inhibited spontaneous emission by a rydberg atom. *Phys. Rev. Lett.*, 55:2137–2140, Nov 1985.

[7] T. L. Nguyen, J. M. Raimond, C. Sayrin, R. Cortiñas, T. Cantat-Moltrecht, F. Assemat, I. Dotsenko, S. Gleyzes, S. Haroche, G. Roux, Th. Jolicoeur, and M. Brune. Towards quantum simulation with circular rydberg atoms. *Phys. Rev. X*, 8:011032, Feb 2018.

[8] Florian Meinert, Christian Hölzl, Mehmet Ali Nebioglu, Alessandro D'Arnese, Philipp Karl, Martin Dressel, and Marc Scheffler. Indium tin oxide films meet circular rydberg atoms: Prospects for novel quantum simulation schemes. *Phys. Rev. Res.*, 2:023192, May 2020.

[9] Sam R. Cohen and Jeff D. Thompson. Quantum computing with circular rydberg atoms. *PRX Quantum*, 2:030322, Aug 2021.

[10] C. Hoelzl, A. Goetzelmann, E. Pultinevicius, M. Wirth, and F. Meinert. Long-lived circular rydberg qubits of alkaline-earth atoms in optical tweezers. *arXiv preprint arXiv:2401.10625*, 2024.

[11] Christoph Fischer. *Quantum Non-Demolition Readout for Optically Trapped Alkaline-Earth Rydberg Atoms.* Theses, ETH Zurich, May 2022.

[12] Andrea Muni, Lea Lachaud, Angelo Couto, Michel Poirier, Raul Celistrino Teixeira, Jean-Michel Raimond, Michel Brune, and Sebastien Gleyzes. Optical coherent manipulation of alkaline-earth circular rydberg states. *Nature Physics*, 18:502–505, 2022.

[13] Thomas F. Gallagher. *Rydberg Atoms.* Cambridge University Press, Cambridge, 1994.

[14] E. M. Purcell, H. C. Torrey, and R. V. Pound. Resonance absorption by nuclear magnetic moments in a solid. *Phys. Rev.*, 69:37–38, Jan 1946.

[15] Daniel Kleppner. Inhibited spontaneous emission. *Phys. Rev. Lett.*, 47:233–236, Jul 1981.

[16] Rodrigo Gastón Cortiñas. *Laser trapped Circular Rydberg atoms for quantum simulation.* Theses, Université Paris sciences et lettres, May 2020.

[17] Wolfgang Demtröder. *Experimentalphysik 3: Atome, Molekuele und Festkoerper.* Springer Spektrum, Berlin, Heidelberg, 5 edition, 2016.

[18] Barton Zwiebach. Fine structure in hydrogen and alkali atoms. `https://bohr.physics.berkeley.edu/classes/221/1112/notes/finestruc.pdf`, 2024.

[19] Immanuel Bloch. Atom- und molekuephysik. Lecture notes for atomic physics.

[20] Thanh Long Nguyen. *Study of dipole-dipole interaction between Rydberg atoms - Toward quantum simulation with Rydberg atoms.* Theses, Université Pierre et Marie Curie UPMC Paris VI, November 2016.

[21] Serge Haroche and Jean-Michel Raimond. *Exploring the Quantum: Atoms, Cavities, and Photons.* Oxford University Press, 2006.

[22] Hans A. Bethe and Edwin E. Salpeter. *Quantum Mechanics of One- and Two-Electron Atoms.* Springer, New York, 1957.

[23] Mireille Aymar, Chris H. Greene, and Eliane Luc-Koenig. Multichannel rydberg spectroscopy of complex atoms. *Rev. Mod. Phys.*, 68:1015–1123, Oct 1996.

[24] John David Jackson. *Classical Electrodynamics.* John Wiley & Sons, 1998.

[25] Christopher C. Gerry and Peter L. Knight. *Introductory Quantum Optics.* Cambridge University Press, Cambridge, 2nd edition, 2023.

[26] Marlan O. Scully and M. Suhail Zubairy. *Quantum Optics.* Cambridge University Press, 1997.

[27] Rodney Loudon. *The Quantum Theory of Light.* Oxford University Press, 3 edition, 2000.

[28] Benjamin Bederson and Herbert Walther. *Advances in Atomic, Molecular, and Optical Physics, Volume 72.* Academic Press, 2023.

[29] Niklas Beisert. Energy and momentum in electrodynamics, 2016. Lecture notes for Electrodynamics.

[30] Niklas Beisert. Radiation in electrodynamics, 2016. Lecture notes for Elektrodynamics.